Title: A cardiac pulse signal affects local field potentials recorded from deep brain stimulation electrodes across clinical targets

Authors:

Katherine R, Tourigny, MD

- Medical Research Council Centre of Research Excellence in Restorative Neural Dynamics, United Kingdom.
- Division of Neurosurgery, Dalhousie University

Rory J, Piper, PhD

- Developmental Neurosciences, UCL Great Ormond Street Institute of Child Health, University College London, 30 Guilford, London, UK, WC1N 1EH.
- Great Ormond Street Hospital for Children NHS Trust, London

Martin, Tisdall, MBBS

- Developmental Neurosciences, UCL Great Ormond Street Institute of Child Health, University College London, 30 Guilford, London, UK, WC1N 1EH.
- Great Ormond Street Hospital for Children NHS Trust, London

Wolf-Julian, Neumann, Dr. med

- Movement Disorder and Neuromodulation Unit, Department of Neurology, Charité – Universitätsmedizin Berlin, corporate member of Freie Universität Berlin and Humboldt-Universität zu Berlin, Chariteplatz 1, 10117 Berlin, Berlin, Germany

Alexander L, Green, PhD

- Nuffield Department of Surgical Sciences, University of Oxford, United Kingdom

Timothy, Denison, PhD

- Medical Research Council Centre of Research Excellence in Restorative Neural Dynamics, United Kingdom
- Institute of Biomedical Engineering, Department of Engineering Science, University of Oxford, Oxford, UK

Joram, van Rheede, DPhil

- Medical Research Council Centre of Research Excellence in Restorative Neural Dynamics, United Kingdom.
- Institute of Biomedical Engineering, Department of Engineering Science, University of Oxford, Oxford, UK

Corresponding Author
Name: Katherine R Tourigny
Current Institution: University of Oxford
Email: katherine.tourigny@sjc.ox.ac.uk

Keywords:

- Local field potential
- Deep brain stimulation
- Artefacts
- Cardiac
- Brain
- Signal processing

Abstract word count: 247
Text word count: 3493
Number of references: 38
Number of tables and/or figures: 8 figures, 3 tables
Number of videos: 0

ABSTRACT

Objective: Many deep brain stimulation (DBS) systems sense local field potentials (LFPs) for patient monitoring or closed-loop therapy (CL-DBS). LFPs can be impacted by artefacts, including a recently discovered cardiac non-electrocardiographic pulse signal that can be visually masked by commercial device filters. We aimed to establish its prevalence across patient groups and brain areas, and to investigate its spectral impact.
Methods: We performed a cross-sectional analysis of LFPs recorded from the cranially mounted Picostim from the pedunculopontine nucleus in multiple systems atrophy patients, periacqueductal gray and sensory thalamus in chronic pain patients, and the centromedian thalamic nucleus (CMT) in paediatric epilepsy patients. For comparison, we analyse externalised recordings from the subthalamic nucleus in Parkinson's disease patients. The PulsAr algorithm was developed to detect and extract pulsatile signals, and we characterised contamination level and spectral content.
Results: Though not visually obvious in CMT, the pulsatile signal was algorithmically detected in all targets, with 33% of LFPs across targets classed as contaminated. Pulse signal power was similar across targets and may have been masked by higher endogenous activity in CMT. While its dominant frequencies were in the heartbeat range, the signal had spectral content extending up to >10Hz.
Conclusions: A heart pulse signal affects LFP recordings from DBS leads across brain regions and patient groups. While masked by some device filters, spectral content can extend into higher (clinically relevant) frequencies. Researchers and clinicians should exercise caution when sensing lower LFP frequencies, especially for automated control of therapy in CL-DBS.

KEY MESSAGES:

What is already known on this topic

- Historically, electrocardiographic artefacts have been a major source of artefact affecting deep brain stimulation recordings, however pulsatile artefact is less well described.

What this study adds

- A cardiac pulse signal affects local field potentials recorded from deep brain stimulation electrodes across clinical targets.
- We introduce an ECG-independent algorithm that detects and extracts this pulsatile signal.
- The heart pulse signal looks like the intracranial pressure waveform and affects spectral frequencies above the heart rate range up to >10Hz.

How this study might affect research, practice, or policy

- Clinicians should incorporate screening and procedures to ensure accurate biomarker detection for clinical decision making.

INTRODUCTION

Deep brain stimulation (DBS) improves symptoms of neurological disorders by modulating pathological neural circuits. It is an established therapy for movement disorders such as Parkinson's disease (PD), dystonia, and essential tremor and for medically refractory epilepsy, with active research underway for other indications[1]. Many DBS devices now incorporate sensing technology to track neural activity around the therapeutic target. In closed loop DBS (CL-DBS), such activity is used to automatically adjust stimulation based on detected neural biomarkers, with the potential to improve efficacy and reduce side effects by maintaining neural activity within an optimal range[1,2]. CL-DBS or adaptive DBS (aDBS) systems have now been approved for human clinical use in epilepsy (NeuroPace Responsive Neurostimulation) and movement disorders (Percept PC, Medtronic)[3–7]. In these systems, the accuracy of the "sensed" neural signal is crucial for achieving effective and safe control of stimulation [8].

Sensing enabled DBS systems measure local field potentials (LFPs), representing the summed electrical activity of a population of neurons[9]. Oscillatory neural activity is often characterized using 'canonical' frequency bands of interest (FOIs) including slow oscillations (< 1 Hz), delta (1–4 Hz), theta (> 4–8 Hz), alpha (> 8–13 Hz), beta (> 13–30 Hz), and gamma (30– 80 Hz)[10]. Certain oscillations have become established neurophysiological biomarkers, such as excessive beta activity in the subthalamic nucleus (STN) in PD which correlates with motor symptoms[11]. Ideally, LFPs are recorded, biomarkers are extracted, and stimulation is adjusted accordingly. However, artefact in LFPs can disrupt biomarker detection and feedback control (figure 1) [12].

Artefact in neural recordings

Artefacts in neural signals originate from non-physiologic (e.g. environment, hardware, stimulation) or physiologic sources with cardiac electrical activity historically most common [12–15]. Electrocardiographic (ECG) contamination with the characteristic 'QRS' shape of the heart's electrical field and methods for its removal are well described[14,16–18]. QRS artefact can arise when the IPG is implanted close to the cardiac dipole and the QRS signal is not rejected as a common mode[12]. Modelling studies predicted that ECG QRS contamination should not affect a cranially mounted IPG such as the Picostim™-DyNeuMo ("Picostim")[12,17,19,20]. However, LFPs recorded with the Picostim in the pedunculopontine nucleus showed a large amplitude repetitive pulse-like signal temporally aligned with ECG but distinct from the well described QRS morphology [21]. Similar repetitive signals have been observed in intraoperative recordings[22]. Leading commercial devices can visually mask this artefact in LFP streams, with default high-pass filter cutoffs ranging from e.g. 1-10 Hz (Medtronic Percept, configurable) or 4-12 Hz (Neuropace RNS) [23–25]. However, this might not remove higher frequency components associated with dynamics of the cardiac cycle, which

could mask neural signals relevant to therapy. The prevalence of this heart pulse signal across the brain remains unclear.

In this paper, we characterize this pulsatile signal in multiple DBS targets and clinical populations and introduce an algorithm to detect it without concurrent ECG measurement. Next, we estimate its spectral content to predict its impact on biomarker frequency bands relevant to (CL-)DBS and assess its relationship to neural signal level and its stability over time.

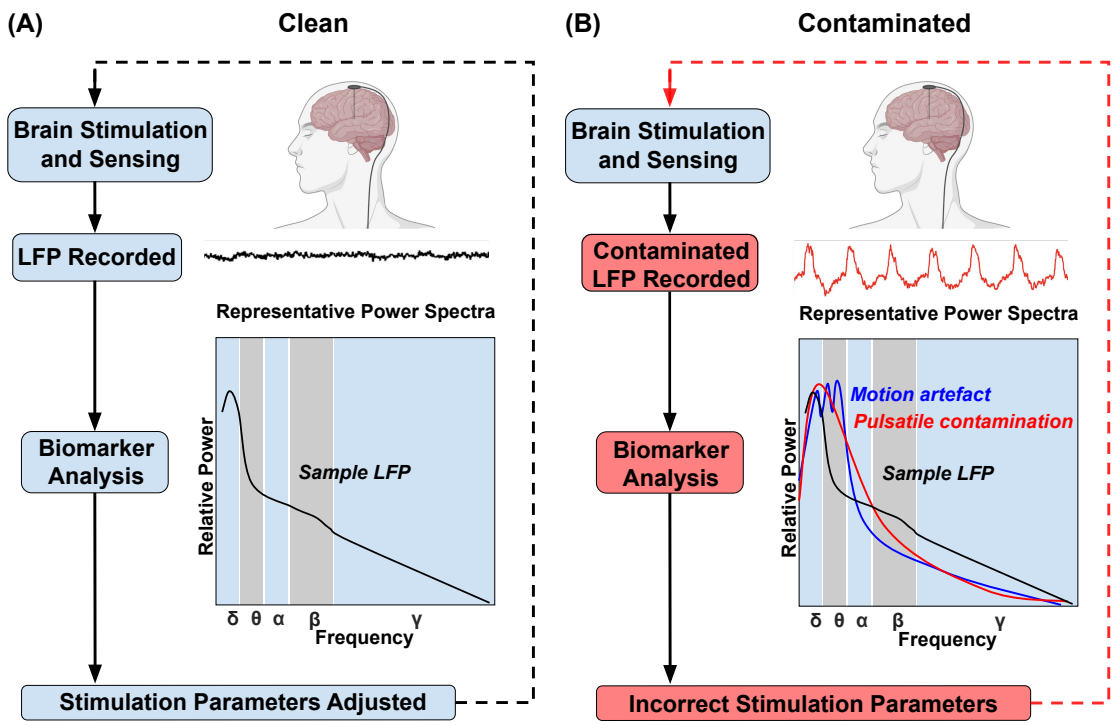

Figure 1. Closed loop DBS with clean and contaminated LFPs. *(A) A clean LFP is recorded, and frequency bands of interest are analyzed for biomarkers. Biomarker levels inform changes to the stimulation parameters through onboard biomarker analysis. New stimulation parameters are sent back to the brain. (B) The LFP is recorded and contaminated by artefact. An example of pulsatile signal is shown in the LFP. Schematic power spectra of a sample LFP, motion artefact, and pulsatile contamination. The power spectra of the artefact may overlap with frequency bands of interest. The onboard analysis may not be able to modify stimulation parameters, may revert to basal stimulation parameters, or may shut down as a safety mechanism.*

METHODS

Data Collection

We performed a retrospective analysis of prospectively collected local field potentials (LFPs) from participants enrolled in adult clinical trials of deep brain stimulation (DBS) of the

pedunculopontine nucleus (PPN) for multiple system atrophy (n = 3, NCT05197816), periaqueductal gray (PAG) and sensory thalamus (ST) DBS for chronic post-stroke pain (n = 3, NCT06387914), as well as a pediatric trial of centromedian nucleus of the thalamus (CMT) DBS for Lennox–Gastaut epilepsy syndrome (n = 3, NCT05437393). These trials utilised the Picostim™-DyNeuMo (referred to as "Picostim") cranially mounted adaptive DBS system (7.4-cc titanium IPG; two 4-contact leads). All LFPs available at the time of analysis were included. Additional subthalamic nucleus (STN) recordings from one adult PD participant were obtained from externalized Medtronic 3389 or SenSight electrodes (Model B33005). Data collection followed each trial's protocol as approved by local ethics boards and regulatory authorities and complied with the Declaration of Helsinki.

LFPs from the PPN, PAG, ST, and CMT were collected using a systematic montage sweep protocol (figure 2). Each sweep consisted of twenty-second bipolar recordings for all possible "within lead" contact pairs with one contact the anode and the other the cathode (contacts 1-4, or 5-8). Longer continuous recordings were available to assess temporal changes in the signal. Picostim recordings were sampled at 1000 Hz. STN recordings were collected from externalized leads at a sampling frequency of 4000 Hz using a Saga64 + (Twente Medical Systems International) device. STN signals were hardware-referenced to the lowermost contact of the DBS electrode and subsequently re-referenced offline in a bipolar configuration.

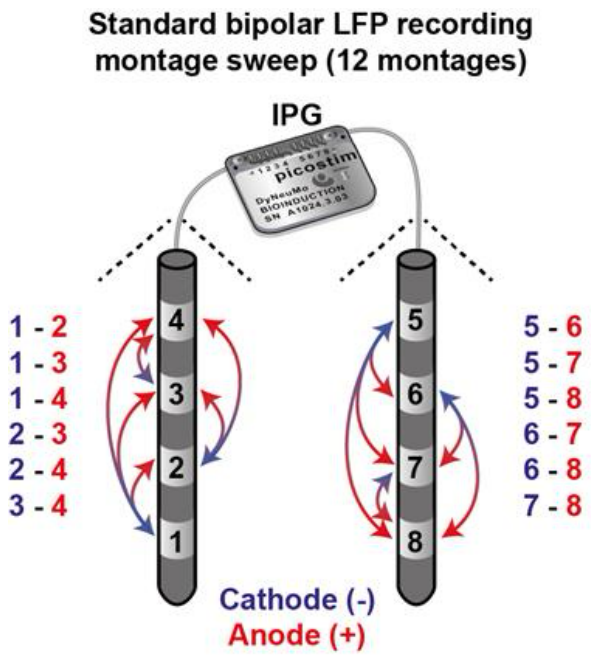

Figure 2. Schematic of the montage trace protocol using the Picostim system and a four-contact electrode. *A twenty second LFP is recorded from all pairwise combinations of contacts sequentially in time. A standard bipolar sensing montage sweep consists of one contact serving as the anode and another as the cathode within the same electrode.*

Signal Processing

Analysis was performed in MATLAB (2023b, Mathworks Inc., Natick, MA, USA). LFPs were filtered with zero-phase, 4th order Butterworth filters: 0.5 Hz high-pass and then a 100Hz low-pass filter. STN signals were then downsampled to 1000Hz. Power spectral densities (PSDs) for LFPs were computed using Welch's method (MATLAB '*pwelch'*, 2000 sample windows, 50% overlap, 0.5 Hz resolution). Fast Fourier transforms (FFT) were used for pulsatile signal templates. A normalized spectral difference was computed at each frequency as the logarithmic ratio between contaminated and clean conditions. Wavelet spectrograms were computed with continuous Morlet wavelet transform (MATLAB *'cwt'*) to allow for scaling of window length to more accurately capture changing frequency content within individual cardiac pulse cycles over time. Two raters (KT, JvR) visually classified traces as "clean" or "contaminated" based on the presence of a large amplitude repetitive pattern repeating at physiologic heart rate[16]. Signals were confirmed free of ECG QRS artefact using an open-source ECG detection and removal toolbox (Perceive, https://github.com/neuromodulation/perceive) [17].

PulsAr algorithm and pulsatile signal characteristics

We developed the PulsAr detection algorithm ("PulsAr") to automatically classify LFPs as clean or contaminated. PulsAr uses cross-correlation to identify highly repetitive features in the signal. Raw LFPs were band-pass filtered between 0.5 Hz and 30 Hz using MATLAB's *highpass* and *lowpass* filters to avoid phase distortion. Autocorrelation was computed for lags up to 10s. After discarding the first one second of signal to remove the zero-lag peak, the root-mean-square (RMS) power of the autocorrelation signal was computed as metric of contamination. Signals were classified as contaminated if they met three criteria: autocorrelation RMS power exceeded the threshold (see below explanation), inter-peak intervals were consistent with physiologic heart rates (50-120 bpm), and there was low variability in this inter-peak interval.

If the LFP was labelled as contaminated, a representative pulsatile template was extracted using a cross-correlation approach adapted from the Perceive toolbox[17]. An initial template was obtained from the autocorrelation peak, and this template cross-correlated with the original signal to identify segments sharing similar morphology. Peaks above 10% of the maximum correlation value and their locations were identified, segments around these peaks extracted, and segments averaged to generate a refined pulsatile template. The template was trimmed to zero-crossings and standardized to allow us to string together a repetitive "pulsatile artefact only" signal. This template was considered the representative pulsatile signal for each contaminated recording. Root mean square (RMS) amplitude was then compared across clean signals, contaminated signals, and pulsatile signal templates across brain regions.

PulsAr performance compared to experimenter ratings was evaluated using receiver operating characteristic (ROC) analysis and a confusion matrix, with consensus visual ratings from KT an JvR as ground truth. We ran PulsAr at 50 thresholds. The optimal threshold of 0.081 when compared to ground truth was used to classify signals for further analysis.

To assess stability of pulsatile signal over time, two PPN recordings over 40 seconds long were segmented into sliding 5-second windows. A pulsatile template was extracted by PulsAr for each 5-second window, and RMS amplitude calculated for each template to qualitatively evaluate within-recording variability.

Statistical Analysis

Inter-rater agreement for visual classification was assessed using Cohen's κ. Power spectral density (PSD) of clean and contaminated local field potentials (LFPs) was computed in linear units; group-level mean spectra and 95% confidence intervals (CI) were converted to decibels (dB) for visualization. Normalized spectral differences were calculated as the logarithmic ratio of contaminated to clean power. Band powers are reported as linear mean ± 95% CI. Differences between clean and contaminated signals were assessed using independent-samples t-tests with Welch's correction, performed separately for each frequency band (delta, theta, alpha, beta, gamma), and corrected for multiple comparisons using the Benjamini–Hochberg (B-H) false discovery rate (FDR, q = 0.05). Root-mean-square (RMS) amplitude is reported as mean ± 95% CI for clean, contaminated, and pulsatile-template signals. Group differences were assessed using one-way ANOVA with Tukey's post hoc correction. Frequency spectra of pulsatile templates are presented as the mean fast Fourier transform (FFT) ± 95% CI for each anatomical area.

RESULTS

Presence of a pulsatile artefact in intracranial LFP data

We visually inspected a total of 433 20 second montage sweep LFP recordings from the cranially mounted Picostim™-DyNeuMo for the presence of a pulsatile artefact. This included recordings from the pedunculopontine nucleus (PPN, n=154, MINDS trial), periacqueductal gray (PAG, n = 12, EPIONE trial), sensory thalamus (ST, n= 12, EPIONE trial), and centromedian thalamus (CMT, n = 255, CADET Pilot). Additionally, we investigated 30 subthalamic nucleus (STN) recordings obtained with externalized leads. Representative clean and contaminated signals from the PPN, PAG, ST, and STN, along with wavelet spectrograms of the contaminated examples, are shown in figure 3. Qualitative inspection showed a clear pulsatile signal in a proportion of PPN, PAG, ST, and STN recordings. In the PPN and PAG, spectrograms showed a prominent power at frequencies corresponding to physiologic heart rate, with spectral components

extending into the 5-10Hz range. The ST and STN had similar but less pronounced patterns. In the PPN and PAG, a second smaller peak in the pulsatile signal can be appreciated. No clear pulsatile signal was seen in the CMT, although three traces were considered potentially contaminated by one rater.

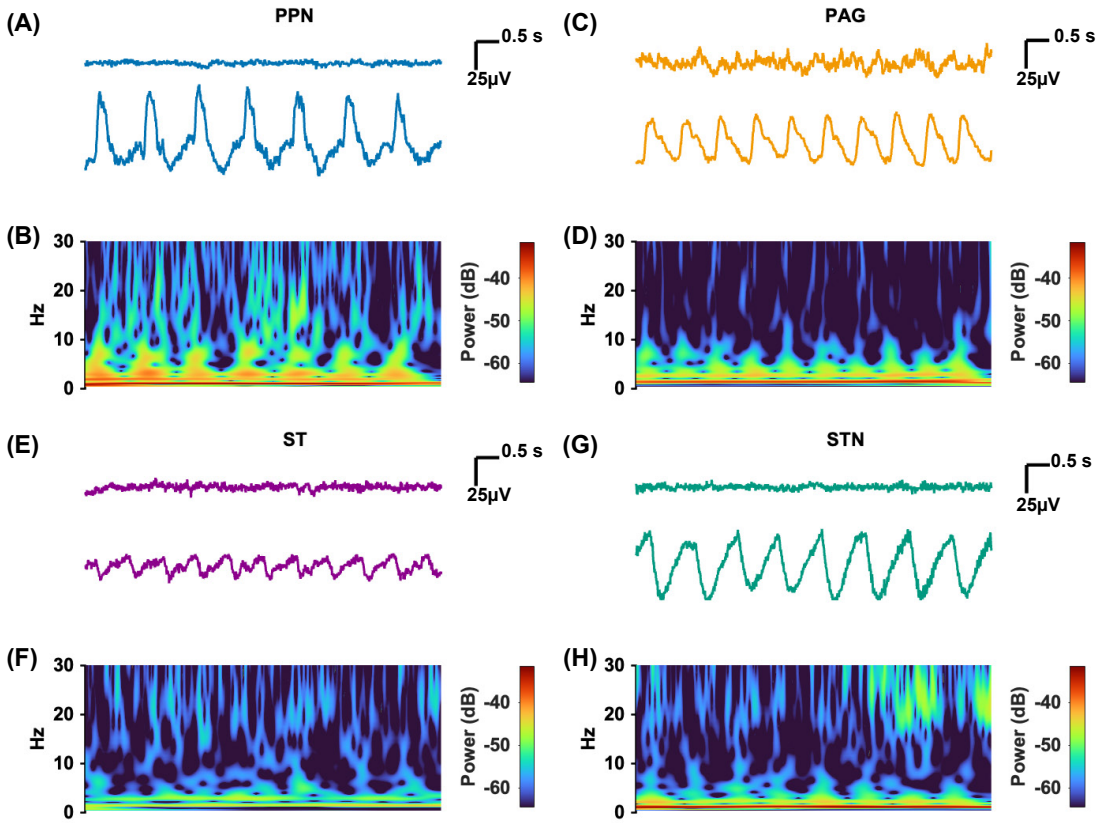

Figure 3. Sample clean and contaminated signals with wavelet spectrograms. *Pulsatile signal morphology was similar across anatomic targets. (A) PPN clean (top) and contaminated (bottom) signals. (B) Wavelet spectrogram showing power of pulsatile signal (dB) in low frequencies and peaks temporally aligned with the peaks seen in the PPN LFP. (C)PAG clean (top) and contaminated (bottom) signals. (D) Wavelet spectrogram showing power of pulsatile signal (dB) in low frequencies and peaks temporally aligned with the peaks seen in the PAG LFP. (E) ST clean (top) and contaminated (bottom) signals. (F) Wavelet spectrogram showing power of pulsatile signal (dB) corresponding with the occurrence of pulsatile waveform in the LFP however less apparent compared to PAG and PPN. (G) STN clean (top) and contaminated (bottom) signals. (H) Wavelet spectrogram showing power of pulsatile signal (dB) corresponding with the occurrence of pulsatile waveform in the LFP however also less apparent than the PPN and PAG. Scalebars apply to all LFP and spectrogram panels. PPN = pedunculopontine nucleus, PAG = periaqueductal grey, ST = sensory thalamus, STN = subthalamic nucleus.*

Across all participants, contamination did not necessarily affect all contact pairs within a montage sweep, and the same pair was not necessarily contaminated across different recording sessions. Overall, rater KT graded 69 traces as contaminated and JvR rated 114 as contaminated. Despite differences in rater conservativeness, inter-rater reliability was high (Cohen's $\kappa = 0.8$).

We developed the PulsAr algorithm to enable objective detection and estimation of pulsatile artefact contamination (figure 4A-D; See Methods). As a ground truth for evaluating algorithm performance, a signal was labelled 'contaminated' if both raters considered a signal contaminated, and 'clean' otherwise. After evaluating 50 thresholds, a RMS contamination threshold of 0.081 optimized algorithm performance (sensitivity 94.2%, specificity 95.1%, F1 score 0.73, and AUC 0.92; figure 4E). This threshold was used to process the final refined dataset.

The final dataset from the clinical trials included 445 montage sweep LFPs: 157 PPN, 84 PAG, 84 ST, and 120 CMT. LFPs from the STN (n = 30) were excluded from prevalence calculations as they were not collected under our standardized montage sweep parameters. The PulsAr algorithm detected contamination in 33% of all LFP recordings, including in 5.8% of CMT recordings which visually looked non-contaminated (Table 1). Sample PulsAr outputs for clean and contaminated signals, ROC, and % contamination results are shown in figure 4.

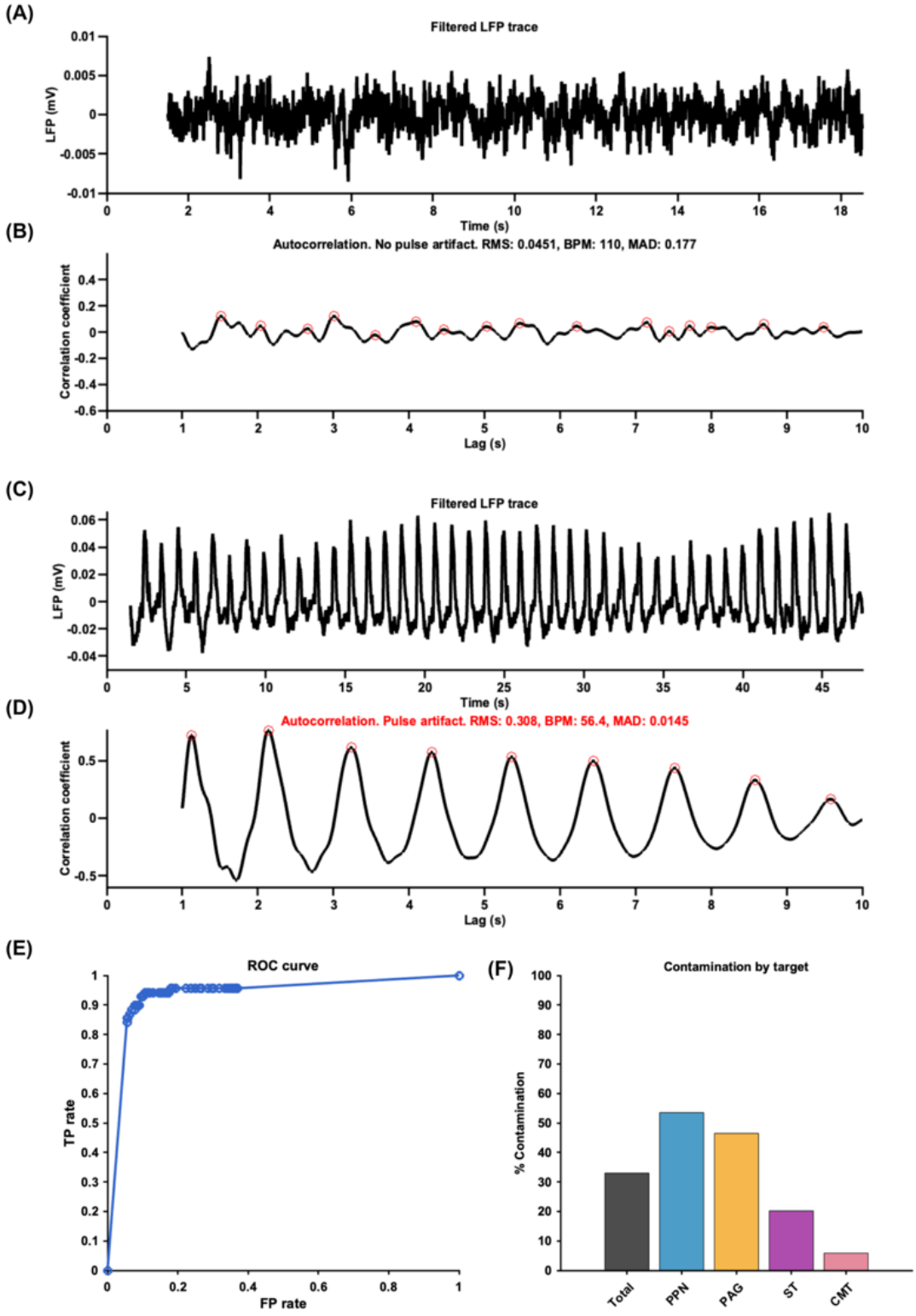
(A)
Filtered LFP trace
LFP (mV)
Time (s)
(B)
Autocorrelation. No pulse artifact. RMS: 0.0451, BPM: 110, MAD: 0.177
Correlation coefficient
Lag (s)
(C)
Filtered LFP trace
LFP (mV)
Time (s)
(D)
Autocorrelation. Pulse artifact. RMS: 0.308, BPM: 56.4, MAD: 0.0145
Correlation coefficient
Lag (s)
(E)
ROC curve
TP rate
FP rate
(F)
Contamination by target
% Contamination
Total
PPN
PAG
ST
CMT

Figure 4. PulsAr output, signal contamination, and algorithm performance. *(A-D) PulsAr algorithm outputs for a clean (A-B) and contaminated (C-D) signals. (A) Clean LFP from the sensory thalamus. (B) Autocorrelation showing no pulsatile signal detected. Autocorrelation step calculates root mean square power (RMS), estimated heart rate in beats per minute (BPM), and mean absolute deviation (MAD). (C) Contaminated LFP from the PPN showing large pulsatile signal. (D) Autocorrelation detected pulsatile signal. (E) Receiver operating characteristics (ROC) curve was calculated by comparing the PulsAr decision with consensus visual inspection from two raters KT and JvR. If the raters did not agree the consensus decision was to label the trace non-contaminated. The PulsAr algorithm was run at 50 different thresholds on all traces to build the ROC curve. (F) Percent of contaminated traces from all traces at each specific target. Overall, 33.0% of the LFPs collected from the Picostim were labelled as contaminated by PulsAr. Of all PPN LFPs 53.5% were contaminated, 46.4% of PAG LFPs, 20.2 % of ST LFPs, and 5.8% of CMT LFPs. RMS = root mean square power, BPM = beats per minute (estimated heart rate), MAD = mean absolute deviation.*

TABLE 1. PulsAr Contamination Results

Anatomic Area	Participants (n)	LFPs Contaminated (n)	Total LFPs (n)	% Contaminated
PPN	3	84	157	53.5
PAG	3	39	84	46.4
ST	3	17	84	20.2
CMT	3	7	120	5.8
Total	**12**	**147**	**445**	**33.0**

**STN (n=1) not included in prevalence calculations*

We next examined how pulsatile signal contamination affects the measurement of common FOIs. For all targets, contaminated signals displayed consistent increases in the lower frequency bands (figure 5). Comparison of power bands between clean versus contaminated signals (Table 2) revealed significant differences in delta power in the PPN (B-H adjusted $p = 0.021$). In the PAG, delta (B-H adjusted $p = 0.014$) and gamma (B-H adjusted $p = 0.025$). In the CMT, significant difference was observed in theta (B-H adjusted $p = 0.025$) and alpha power (B-H adjusted $p = 0.025$). There were no significant differences in FOIs in either the ST or STN.

Table 2. Band power differences in clean vs contaminated LFPs per DBS target

Anatomy	Band	Mean band power (mV^2/Hz) [95% CI]		p - value	Adjusted p-value
		Clean	Contaminated		
PPN	Delta	3.6×10^{-6} [1.8×10^{-6}, 5.5×10^{-6}]	1.1×10^{-5} [6.4×10^{-6}, 1.6×10^{-5}]	*0.0041	*0.021
	Theta	6.5×10^{-7} [4.2×10^{-7}, 8.7×10^{-7}]	6.6×10^{-7} [4.3×10^{-7}, 8.9×10^{-7}]	0.95	0.95
	Alpha	2.2×10^{-7} [1.6×10^{-7}, 2.8×10^{-7}]	2.1×10^{-7} [1.5×10^{-7}, 2.7×10^{-7}]	0.85	0.95
	Beta	7.3×10^{-8} [5.7×10^{-8}, 8.9×10^{-8}]	6.1×10^{-8} [5.3×10^{-8}, 7.0×10^{-8}]	0.21	0.525
	Gamma	1.9×10^{-8} [1.7×10^{-8}, 2.2×10^{-8}]	1.8×10^{-8} [1.7×10^{-8}, 2.0×10^{-8}]	0.36	0.6
PAG	Delta	2.7×10^{-6} [2.1×10^{-6}, 3.2×10^{-6}]	7.3×10^{-6} [4.4×10^{-6}, 1.0×10^{-5}]	*0.0027	*0.014
	Theta	6.1×10^{-7} [4.9×10^{-7}, 7.3×10^{-7}]	5.9×10^{-7} [4.4×10^{-7}, 7.4×10^{-7}]	0.84	0.84
	Alpha	2.3×10^{-7} [1.9×10^{-7}, 2.6×10^{-7}]	2.0×10^{-7} [1.6×10^{-7}, 2.3×10^{-7}]	0.22	0.28
	Beta	7.2×10^{-8} [6.3×10^{-8}, 8.2×10^{-8}]	5.8×10^{-8} [4.9×10^{-8}, 6.8×10^{-8}]	0.034	0.057
	Gamma	2.0×10^{-8} [1.8×10^{-8}, 2.2×10^{-8}]	1.6×10^{-8} [1.4×10^{-8}, 1.8×10^{-8}]	0.01	*0.025
ST	Delta	1.7×10^{-6} [1.1×10^{-6}, 2.3×10^{-6}]	3.7×10^{-6} [1.7×10^{-6}, 5.7×10^{-6}]	0.056	0.14
	Theta	3.3×10^{-7} [2.6×10^{-7}, 4.1×10^{-7}]	3.2×10^{-7} [1.8×10^{-7}, 4.6×10^{-7}]	0.85	0.85
	Alpha	1.4×10^{-7} [1.1×10^{-7}, 1.6×10^{-7}]	1.2×10^{-7} [6.1×10^{-8}, 1.8×10^{-7}]	0.60	0.75
	Beta	6.2×10^{-8} [5.4×10^{-8}, 7.0×10^{-8}]	5.2×10^{-8} [3.6×10^{-8}, 6.8×10^{-8}]	0.24	0.4
	Gamma	2.3×10^{-8} [2.2×10^{-8}, 2.4×10^{-8}]	1.9×10^{-8} [1.6×10^{-8}, 2.2×10^{-8}]	0.024	0.12
CMT	Delta	4.0×10^{-5} [3.1×10^{-5}, 5.0×10^{-5}]	4.9×10^{-5} [1.8×10^{-5}, 8.0×10^{-5}]	0.55	0.69
	Theta	1.9×10^{-5} [1.4×10^{-5}, 2.4×10^{-5}]	7.8×10^{-6} [1.3×10^{-6}, 1.4×10^{-5}]	*0.0069	*0.025
	Alpha	3.9×10^{-6} [2.6×10^{-6}, 5.2×10^{-6}]	1.8×10^{-6} [6.0×10^{-7}, 2.9×10^{-6}]	0.01	*0.025
	Beta	5.6×10^{-7} [4.5×10^{-7}, 6.8×10^{-7}]	4.8×10^{-7} [2.5×10^{-7}, 7.2×10^{-7}]	0.50	0.69
	Gamma	3.2×10^{-8} [2.8×10^{-8}, 3.5×10^{-8}]	3.2×10^{-8} [2.3×10^{-8}, 4.1×10^{-8}]	0.86	0.86
STN	Delta	1.6×10^{-6} [4.8×10^{-7}, 2.8×10^{-6}]	1.8×10^{-5} [5.8×10^{-6}, 3.0×10^{-5}]	0.01	0.05
	Theta	2.2×10^{-7} [8.0×10^{-8}, 3.6×10^{-7}]	1.9×10^{-7} [1.4×10^{-7}, 2.4×10^{-7}]	0.67	0.67
	Alpha	2.7×10^{-7} [9.7×10^{-8}, 4.5×10^{-7}]	2.1×10^{-7} [1.2×10^{-7}, 3.0×10^{-7}]	0.46	0.58
	Beta	7.4×10^{-7} [2.4×10^{-7}, 1.2×10^{-6}]	3.5×10^{-7} [2.1×10^{-7}, 4.8×10^{-7}]	0.12	0.3
	Gamma	3.6×10^{-8} [1.4×10^{-8}, 5.8×10^{-8}]	2.3×10^{-8} [2.0×10^{-8}, 2.7×10^{-8}]	0.22	0.37

** P-values were adjusted for multiple comparisons across frequency bands using the Benjamini–Hochberg (B-H) false discovery rate (FDR) procedure.*

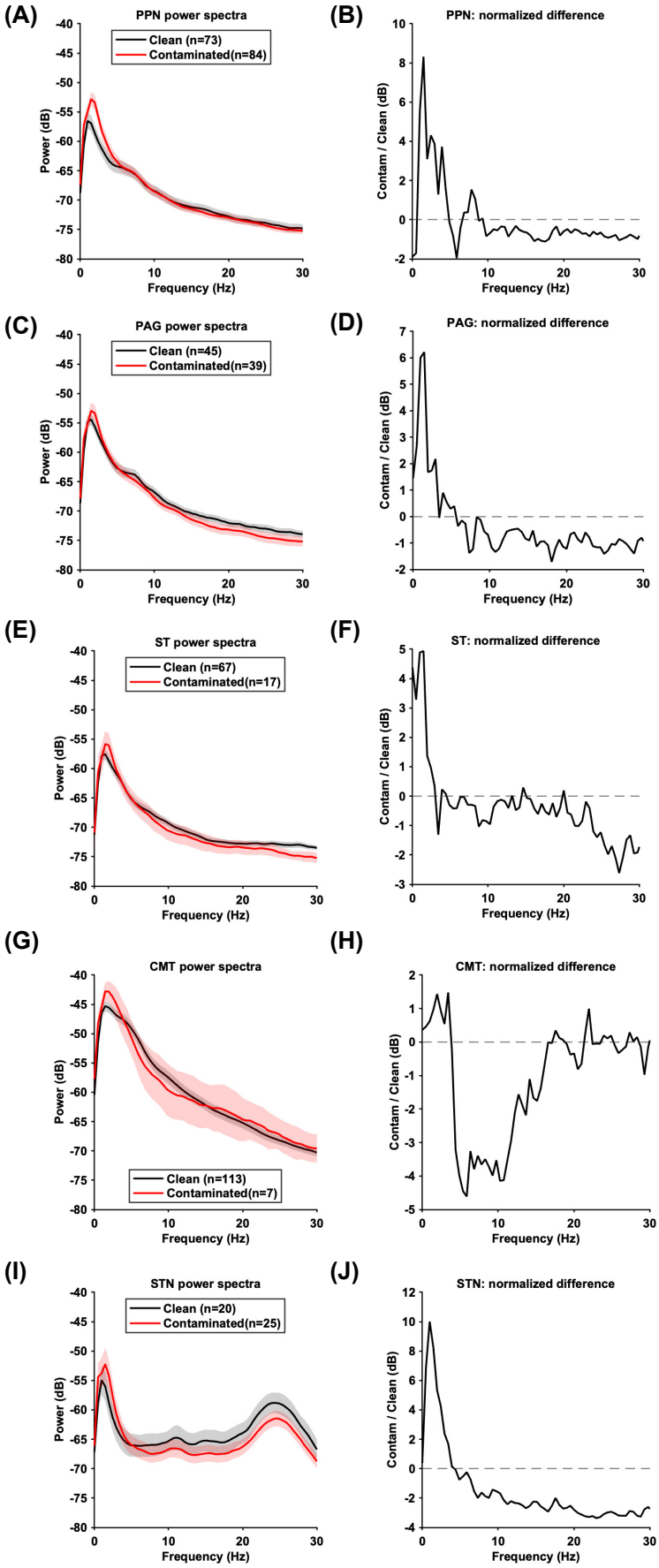
(A)
PPN power spectra
Clean (n=73)
Contaminated(n=84)
Power (dB)
Frequency (Hz)
(B)
PPN: normalized difference
Contam / Clean (dB)
Frequency (Hz)
(C)
PAG power spectra
Clean (n=45)
Contaminated(n=39)
Power (dB)
Frequency (Hz)
(D)
PAG: normalized difference
Contam / Clean (dB)
Frequency (Hz)
(E)
ST power spectra
Clean (n=67)
Contaminated(n=17)
Power (dB)
Frequency (Hz)
(F)
ST: normalized difference
Contam / Clean (dB)
Frequency (Hz)
(G)
CMT power spectra
Clean (n=113)
Contaminated(n=7)
Power (dB)
Frequency (Hz)
(H)
CMT: normalized difference
Contam / Clean (dB)
Frequency (Hz)
(I)
STN power spectra
Clean (n=20)
Contaminated(n=25)
Power (dB)
Frequency (Hz)
(J)
STN: normalized difference
Contam / Clean (dB)
Frequency (Hz)

Figure 5. Power spectra of clean and contaminated LFPs. *Power spectra and normalized spectral differences in clean and contaminated power spectral density (PSD) for clean and contaminated LFPs for the PPN (A, B), PAG (C,D), ST (E,F), CMT (G,H), STN (I,J). Mean power spectral densities were first calculated by averaging in linear power units. A normalized spectral difference was then computed at each frequency as the logarithmic ratio between contaminated and clean conditions. The PPN, PAG, ST, and STN plots show contamination produced frequency-dependant increases in spectral power with maximal effects in low frequencies. This difference was significant for delta frequencies in the PPN (B-H adjusted p = 0.0.021) and PAG (B-H adjusted p = 0.014 and gamma in the PAG (B-H adjusted p = 0.025). There were no significant differences in the ST or STN. In the CMT there was significantly lower spectral power in the theta (B-H adjusted p = 0.0069 and alpha power in contaminated traces. B-H adjusted = Benjamini-Hochberg adjusted, PPN = pedunculopontine nucleus, PAG = periaqueductal gray, ST = sensory thalamus, CMT = centromedian nucleus of the thalamus, STN = subthalamic nucleus.*

Artefact characteristics

PulsAr reliably extracted pulsatile templates from contaminated LFPs. A sample output of the first and second cross correlations and pulsatile signal template extraction is shown in figure 6A-B. For each contaminated LFP, the pulsatile template was extracted, frequency spectra inspected, and templates stitched together in repeats to form a pulsatile template string independent of underlying LFP activity (figure 6 C, E, G, I, K). Spectral analysis of the templates showed they predominantly contained frequencies in the delta power band.

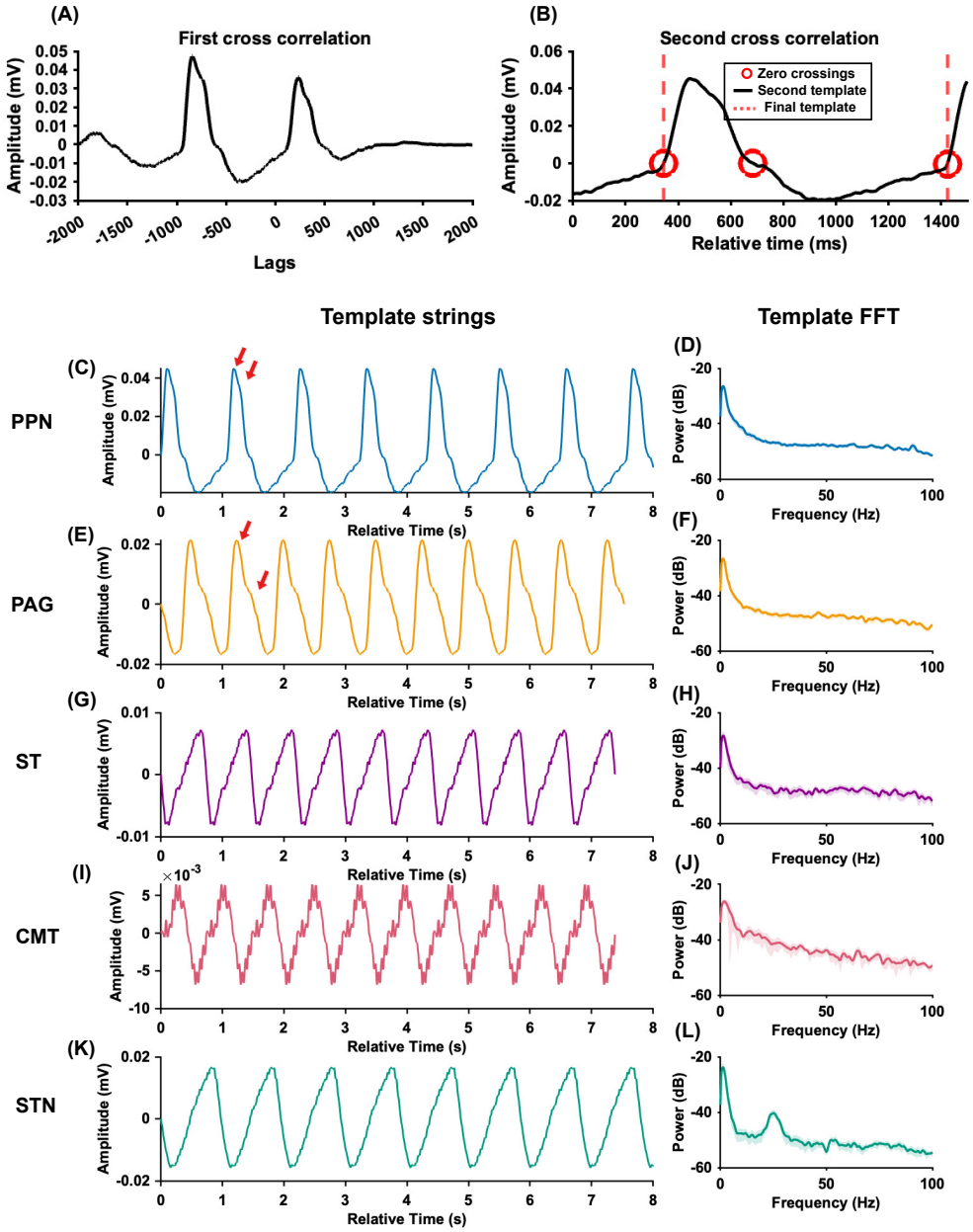

Figure 6. Pulsatile signal detection, extraction, and frequency content evaluation. *(A) A sample output from the extraction element of the PulsAr algorithm. In the first cross correlation, the signal is cross correlated with itself to identify areas of high correlation, a repeating shape in the signal. The area with highest correlation is mapped back to the signal to extract a first template shape. (B) The first template is cross correlated with the original signal again and areas of highest correlation are extracted and averaged together to form the second template. For later processing, and to prevent square waves, we select where the signal crosses zero. The final template is then used to make strings of artefact. (C) Pulsatile waveform strings extracted from a sample PPN LFP. (D) Mean +/- 95% CI of the fast Fourier transform (FFT) of templates extracted from all contaminated PPN signals. Red arrows indicate primary and secondary peak morphology resembling P1 and P2 in an intracranial pressure waveform. (E) Pulsatile waveform strings extracted from a sample PAG LFP. Red arrows indicate primary and secondary peak morphology*

resembling P1 and P2 in an intracranial pressure waveform. (F) Mean +/- 95% CI of the FFT of templates extracted from all contaminated PAG signals. (G) Pulsatile waveform strings extracted from a sample ST LFP. (H) Mean +/- 95% CI of the FFT of templates extracted from all contaminated ST signals. (I) Pulsatile waveform strings extracted from a sample CMT LFP. (J) Mean +/- 95% CI of the FFT of templates extracted from all contaminated CMT signals. (K) Pulsatile waveform strings extracted from a sample STN LFP. (L) Mean +/- 95% CI of the FFT of templates extracted from all contaminated STN signals. PPN = pedunculopontine nucleus, PAG = periaqueductal grey, ST = sensory thalamus, CMT = centromedian nucleus of the thalamus, STN = subthalamic nucleus.

We sought to determine why PulsAr detected contamination in CMT LFPs despite no visual pulsatile waveform. We compared RMS amplitudes of clean, contaminated, and extracted pulsatile signal templates from LFPs within each brain region (figure 7A). A one-way ANOVA revealed a significant effect of condition on RMS values in the PPN, PAG, ST, and CMT with Tukey–Kramer post-hoc test determining significance between groups (Table 3). No significant differences were found in the STN. In the CMT, signal RMS amplitudes calculated from contaminated LFPs were no different than clean, but both were significantly larger than that of the pulsatile template. This suggests that a pulsatile component, if present, is small compared to endogenous CMT signal potentially making it visually undetectable. Finally, the pulsatile signal was not always stable over time. In two 40-second PPN recordings, sliding-window analysis showed how the RMS amplitude of the artefact component can fluctuate even over relatively short timescales (figure 7B).

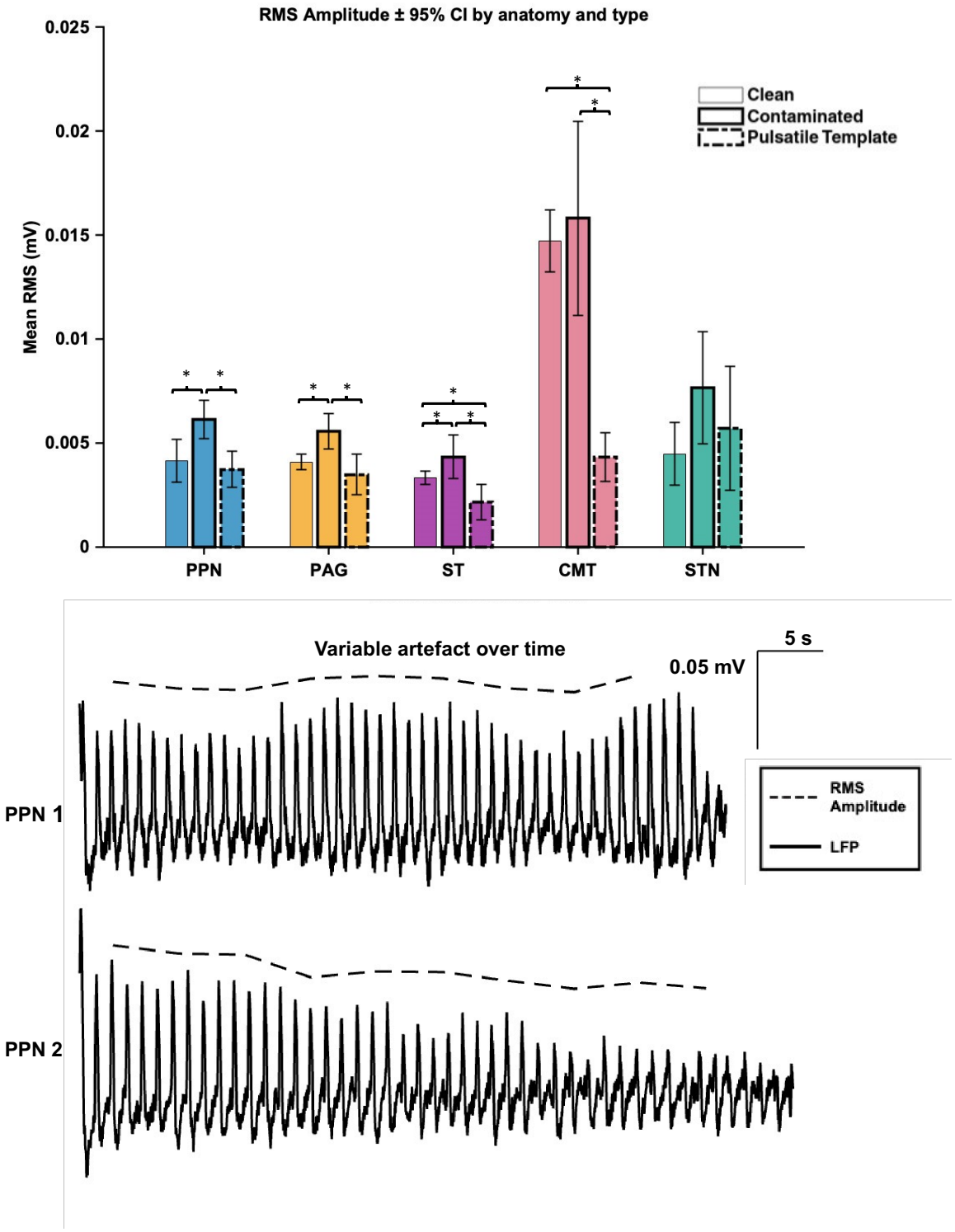

Figure 7. Comparative RMS amplitudes of signals and extracted pulsatile templates. *(A) Mean RMS amplitude of clean, contaminated, and isolated pulsatile templates from each DBS target region. Error bars represent 95% CI. All areas had a significant difference between the contaminated signals and pulsatile template signals. Only the*

*CMT had no significant difference between clean and contaminated signals. (B) RMS amplitudes of pulsatile templates extracted are not necessarily stable over time. Two sample contaminated signals are presented. RMS amplitude was calculated for five second segments using a sliding window on the contaminated signal. The RMS amplitude follows the observed pulsatile signal within the LFP. *Iindicates significance.*

Table 3. RMS amplitude comparisons between extracted pulsatile signal templates, and clean and contaminated LFPs

Anatomy	Classification	Mean RMS (mV) +/- 95% CI	p value	Significance Letter
PPN	Clean	0.0041 (0.0031–0.0052)	0.00064	a
	Contaminated	0.0061 (0.0052–0.0070)		b
	Pulsatile Template	0.0037 (0.0029–0.0046)		a
PAG	Clean	0.0041 (0.0037–0.0044)	0.00056	a
	Contaminated	0.00556 (0.0047–0.0064)		b
	Pulsatile Template	0.0035 (0.0025–0.0045)		a
ST	Clean	0.0033 (0.0030–0.0036)	0.00030	a
	Contaminated	0.0043 (0.0033–0.0054)		b
	Pulsatile Template	0.0022 (0.0013–0.0030)		c
CMT	Clean	0.015 (0.013–0.016)	0.0025	a
	Contaminated	0.016 (0.011–0.020)		a
	Pulsatile Template	0.0043 (0.0031–0.0055)		b
STN	Clean	0.0045 (0.0030, 0.0060)	0.26	a
	Contaminated	0.0077 (0.0050, 0.010)		a
	Pulsatile Template	0.0057 (0.0027, 0.0087)		a

Significance letters denote results of Tukey post-hoc comparisons following one-way ANOVA within each anatomical region. Groups sharing the same letter are not significantly different ($p > 0.05$).

DISCUSSION

Here we described and characterized a pulsatile signal present in intracranial LFP recordings from DBS leads. We showed that this signal affects recordings across multiple DBS targets and can particularly affect estimates of lower frequency LFP power. Our detection and template reconstruction algorithms enable screening and reconstruction of this artefact without access to ground truth ECG data, providing practical tools for assessing data quality. In the context of CL-DBS, the pulsatile cardiac signal may interfere with neural biomarkers of interest, disrupting adaptive control. Screening DBS recordings for pulsatile contamination is therefore essential for both data interpretation and safe CL-DBS implementation.

Pulsatile signal prevalence

Our work expands on prior observations of cardiac pulse-synchronous contamination in neural recordings[21,22]. We identified pulsatile signals across multiple DBS targets, neurological conditions, and in two recording setups (a cranially mounted IPG and an externalized lead

recording system). Furthermore, we developed an ECG-independent classifier, PulsAr, that reliably identifies contaminated LFPs and extracts representative pulsatile waveform templates. PulsAr showed high sensitivity and specificity relative to visual ratings, which are stable to class imbalance. Frequency-dependent metrics such as accuracy and precision were influenced by the unequal distribution of clean and contaminated traces.

Across montage sweeps, 33.0% of LFPs were contaminated, increasing to 43.1% when excluding the largely clean CMT. In other areas, contamination patterns varied across contacts and sessions. This instability complicates mitigation strategies for CL-DBS based on constant correction factors or contact selection. Because contamination occurred across diseases, age groups, and anatomic areas, the pulsatile signal likely reflects a brain-wide phenomenon across populations.

Although PulsAr identified contamination in a small number of CMT traces, no clear pulsatile waveform was visible. RMS amplitude analysis suggests this may reflect masking by relatively large endogenous CMT signals. Another possibility is PulsAr detection of other repetitive patterns, such as spike-and-wave discharges [26]. Simultaneous LFP–ECG recordings will be necessary to determine whether the CMT contamination is cardiac-related. Differences in surgical technique, such as the use of a guide tube that remained in place in the CADET Pilot (Renishaw neuroguide™ DBS electrode delivery system, UK) may also reduce movement of the electrode and therefore LFP contamination.

We considered why this pulsatile signal may have gone previously unrecognized. High pass filters on commercial systems like Medtronic's Percept™ PC device and Neuropace's RNS system may remove the more visually obvious components of the pulsatile artefact [23–25]. Our 0.5 Hz high-pass drift removal filter preserved lower-frequency content and enabled clear visualization and detection of the pulsatile waveform. The PulsAr detector was intentionally designed to identify signals repeating at heart-rate frequencies (0.83–2 Hz).

Pulsatile signal characteristics

The absence of an ECG QRS signature aligns with prior modeling predictions that cranially mounted systems should not see interference from the cardiac dipole [17]. Instead, the pulsatile signal showed a morphology similar to intracranial pressure (ICP) waveforms, with a primary and sometimes a secondary peak[27]. The extracted pulsatile signals contained frequencies up to at least 5-10 Hz and was dynamic over time, complicating removal without data loss. A peak in the beta band was seen in the extracted pulsatile template from the STN which could be due to prominence of beta in this region interacting with our template extraction algorithm, or due to referencing.

Consistent with the dominant low frequency content of the heart pulse signal, PPN and PAG had significantly different delta band power between clean and contaminated signals. Delta band activity is implicated in various physiologic and pathologic brain states [28]. The presence of pulsatile contamination must be considered in future LFP studies targeting these regions. Contaminated CMT recordings showed a small decrease in theta and alpha band power, suggesting a non-additive interaction of artefact and true signal. This could reflect increased likelihood of artefact detection against certain types of background activity; however, interpretation is limited by the small artefact magnitude with respect to the signal and small number of contaminated traces.

Mechanism of pulsatile artefact generation

A key question is the source of this pulsatile signal. We hypothesize that cardiac-driven brain pulsatility generates pulse-synchronous LFP components via electromechanical coupling (figure 8)[29]. This brain pulsatility is due to cyclic changes in the volumes of the vascular and cerebrospinal fluid compartments compensate for one another to maintain intracranial pressure within a safe range. Brain pulsations coupled to the cardiac cycle can be seen in the fontanelle of newborns, on phase-gated MRI, and intraoperative visualization [27,30–33]. The morphologic similarity of the waveform in contaminated tracts (3A&C) to an ICP waveform, with a first (P1) and sometimes second peak (P2), supports a mechanical origin[27]. The fact that an analogous P1 and P2 were captured in the extracted pulsatile templates suggest it is a common feature captured during the averaging process (6C&E). Higher contamination rates in the brainstem-adjacent regions, PPN and PAG, is consistent with known spatial gradients in brain pulsatility[34].

Additional mechanisms may include electrode micromotion or streaming potentials from pulsatile ionic blood flow (figure 8) [35]. Electromechanical coupling differences due to anatomic location or proximity to vessels or CSF spaces, may contribute and require further investigation. Given the 'macro' scale of brain pulsations, it is interesting that pulsatile artefact is not rejected as a common mode and is present in bipolar recordings. Differential amplification may convert small asymmetries in electrode deformation into measurable voltage differences, explaining variable contamination patterns.

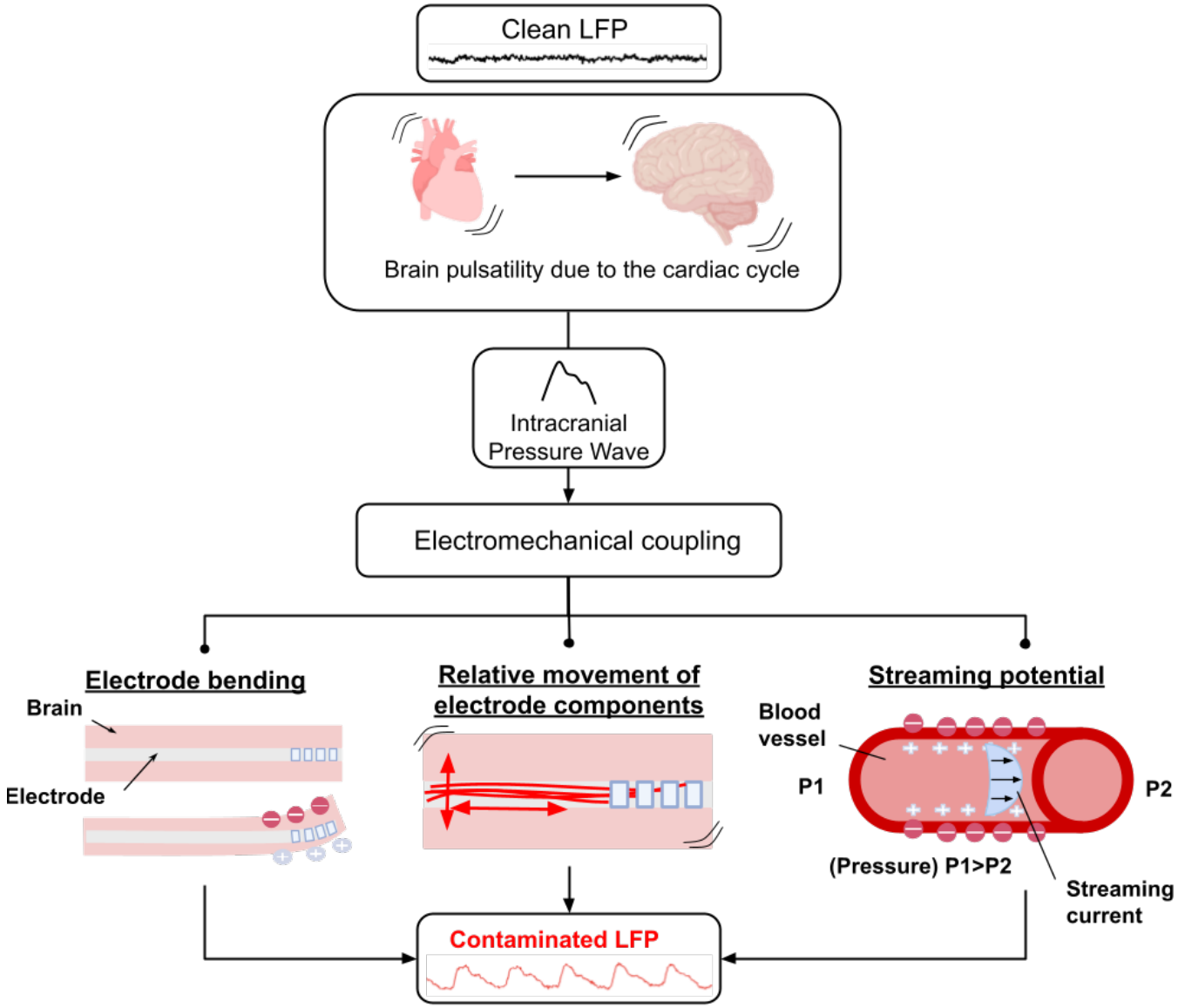

Figure 8. Mechanisms of pulsatile signal generation related to the cardiac cycle. *A schematic showing the hypothesized process of generating an LFP contaminated with pulsatile signal. The brain pulses during the cardiac cycle due to systolic arterial blood volume causing compensatory changes in intracranial CSF volume. This can be measured as an intracranial pressure wave. We hypothesize that electromechanical coupling causes the generation of the pulsatile signal. This could be due to electrode bending and impedance changes, the relative movement of electrode components (such as the wires within the lead causing a relative change in the perceived voltage), or a streaming potential.*

Clinical implications and potential use as a tool

Pulsatile contamination poses challenges for CL-DBS. We show high-pass filtering alone may be insufficient given pulsatile contamination in our spectrograms extending to >10 Hz (Fig. 3). This signal may affect clinical decisions, causing false threshold crossings and unintended stimulation. Intracranial pulsatility exhibits oscillations beyond the fundamental heart-rate frequency further supporting a pulsatility hypothesis[12,27]. Future studies of low frequency oscillatory activity using DBS systems should be aware that LFPs may be affected by heart rate or intracranial pressure and compliance (also affected by e.g. posture). This is particularly important in long term band power tracking where the underlying full spectrum timeseries is not saved, preventing post-hoc screening for cardiac contamination.

PulsAr provides an objective, ECG independent screening tool and could support online monitoring or contact selection in the future. An intriguing possibility is that the PulsAr detector and pulsatile signals in LFPs could be repurposed as a clinical tool, for example as a heart-rate estimator for sleep staging, seizure-related tachycardia detection, or as a proxy for intracranial dynamics.

Limitations and future directions

PulsAr is designed to detect large amplitude, regularly repeating signals at physiological heart rate frequencies, and therefore by definition is vulnerable to false positives if such signals are present in underlying neural activity. Simultaneous ECG-LFP recordings are needed to validate PulsAr as an intracranial heart rate detector for specific clinical targets and to control for this effect. In our case, simultaneous ECG and LFP recordings will be required to confirm whether contamination detected by PulsAr in the CMT is cardiac related. Further longitudinal data is required to determine if there is chronic contamination patterns among contact pairs. ICP and brain pulsatility is known to change with position and during sleep and it would be interesting to investigate the effect of position on the pulsatile signal[31,32,36–38]. Finally, determining the electromechanical mechanism generating the pulsatile signal might allow for design of DBS technology that is less sensitive to cardiac pulse contamination.

CONCLUSIONS

We demonstrate that heart pulse signal is present in recordings from DBS leads across multiple targets and clinical populations. While the most obvious components may be filtered out by commercial device streaming filters, it affects frequencies above heart rate and could affect biomarkers used for clinical decisions. Our ECG-independent detector reliably identifies and extracts this signal. Broadband spectral content and temporal variability complicate automated removal. Recognising and mitigating pulsatile contamination is essential for accurate sensing and

safe closed-loop therapy. Further work is needed to clarify its physiological origin and clinical significance.

ACKNOWLEDGMENTS

We acknowledge contributions of the clinical teams involved in trial design and data collection. For the MINDS trial, we thank Alceste Deli, Robert Toth, Mayela Zamora, and Amir P. Divanbeighi Zand. For EPIONE, we acknowledge Victoria Marks, Rachel Crockett, John Eraifej, and Martin Gillies. For CADET Pilot, we thank Martin Tisdall, Marios Kaliakatsos, Antonio Valentin, Victoria Marks, John Fleming, Sarah Carter, Friederike Moeller, and Rory Piper.

AUTHOR CONTRIBUTIONS

Conceptualization**:** KT, JvR, TD; Methodology**:** KT and JvR; Data Collection**:** TD, MT, AG, JN, RP, JvR; Data Analysis**:** KT, JvR; Writing**:** KT, JvR; Review & Editing**:** KT, JvR, TD, MT, AG, WJN, RP

FUNDING AND DISCLOSURES

KT is funded through the Clarendon Scholarship (University of Oxford), and the Dr. Patrick Madore Clinical Investigator Traineeship (Dalhousie University). TD has funding through the Royal Academy of Engineering Chair in Emerging technologies and Medical Research Council grants MC_UU_00003/3. TD, MT, RP, and JvR have funding through NIHR Invention for Innovation (i4i) NIHR205474. MT and RP have funding through the Royal Academy of Engineering. RP has funding through NIHR and GOSH Children's Charity. AG received funding from the Jon Moulton Charity Trust. WJN received funding from the European Union (ERC, ReinforceBG, project 101077060), Deutsche Forschungsgemeinschaft (DFG, German Research Foundation) – Project-ID 424778381 – TRR 295 and the Bundesministerium für Bildung und Forschung (BMBF, project FKZ01GQ1802).

KT, RP, and MT have no disclosures to declare. TJD is a founder and chief engineer of Amber Therapeutics Ltd., is the non-executive chairman of Mint Neurotechnologies Ltd, and a non-executive director at Onward Medical N.V. JvR has received speaker fees from Medtronic in 2023 and has acted as a paid consultant for Amber Therapeutics Ltd. in 2025. AG is a founding member of Amber Therapeutics and a consultant with Abbott. WJN received honoraria for consulting from InBrain – Neuroelectronics that is a neurotechnology company and honoraria for talks from Medtronic that is a manufacturer of deep brain stimulation devices unrelated to this manuscript.

DATA AVAILABILITY

Code will be released on manuscript acceptance following peer review. The dataset is not yet openly available as it is being used in ongoing projects. Due to data protection regulations access to the raw data would need to be in a trusted research environment as part of a collaboration. Please contact katherine.tourigny@sjc.ox.ac.uk.

REFERENCES

1 Krauss JK, Lipsman N, Aziz T, *et al.* Technology of deep brain stimulation: current status and future directions. *Nat Rev Neurol*. 2021;17:75–87. doi: 10.1038/s41582-020-00426-z

2 Lozano AM, Lipsman N, Bergman H, *et al.* Deep brain stimulation: current challenges and future directions. *Nat Rev Neurol*. 2019;15:148–60. doi: 10.1038/s41582-018-0128-2

3 Bronte-Stewart H, Beudel M, Ostrem JL, *et al.* Adaptive DBS Algorithm for Personalized Therapy in Parkinson's Disease: ADAPT-PD clinical trial methodology and early data (P1-11.002). *Neurology*. 2023;100:3204. doi: 10.1212/WNL.0000000000203099

4 Jimenez-Shahed J. Device profile of the percept PC deep brain stimulation system for the treatment of Parkinson's disease and related disorders. *Expert Rev Med Devices*. 2021;18:319–32. doi: 10.1080/17434440.2021.1909471

5 Stanslaski S, Herron J, Chouinard T, *et al.* A Chronically Implantable Neural Coprocessor for Investigating the Treatment of Neurological Disorders. *IEEE Trans Biomed Circuits Syst*. 2018;12:1230–45. doi: 10.1109/TBCAS.2018.2880148

6 Stanslaski S, Summers RLS, Tonder L, *et al.* Sensing data and methodology from the Adaptive DBS Algorithm for Personalized Therapy in Parkinson's Disease (ADAPT-PD) clinical trial. *npj Parkinsons Dis*. 2024;10:174. doi: 10.1038/s41531-024-00772-5

7 Sun F, Morrell M. The RNS System: responsive cortical stimulation for the treatment of refractory partial epilepsy - PubMed. *Expert Rev Med Devices*. Published Online First: 2014. doi: 10.1586/17434440.2014.947274

8 Parastarfeizabadi M, Kouzani A. Advances in closed-loop deep brain stimulation devices. *Journal of NeuroEngineering and Rehabilitation*. 2017;14. doi: 10.1186/s12984-017-0295-1

9 Herreras O. Local Field Potentials: Myths and Misunderstandings. *Front Neural Circuits*. 2016;10. doi: 10.3389/fncir.2016.00101

10 Bouthour W, Mégevand P, Donoghue J, *et al.* Biomarkers for closed-loop deep brain stimulation in Parkinson disease and beyond. *Nat Rev Neurol*. 2019;15:343–52. doi: 10.1038/s41582-019-0166-4

11 Brown P. Oscillatory nature of human basal ganglia activity: Relationship to the pathophysiology of Parkinson's disease. *Movement Disorders*. 2003;18:357–63. doi: 10.1002/mds.10358

12 Sorkhabi MM, Benjaber M, Brown P, *et al.* Physiological Artefacts and the Implications for Brain-Machine-Interface Design. Bioengineering 2020. doi: 10.1109/SMC42975.2020.9283328

13 Swann NC, de Hemptinne C, Miocinovic S, *et al.* Chronic multisite brain recordings from a totally implantable bidirectional neural interface: experience in five patients with Parkinson's disease. *J Neurosurg*. 2018;128:605–16. doi: 10.3171/2016.11.JNS161162

14 Hammer LH, Kochanski RB, Starr PA, *et al.* Artifact characterization and a multipurpose template-based offline removal solution for a sensing-enabled deep brain stimulation device. *Stereotact Funct Neurosurg*. 2022;100:168–83. doi: 10.1159/000521431

15 van Rheede JJ, Feldmann LK, Busch JL, *et al.* Diurnal modulation of subthalamic beta oscillatory power in Parkinson's disease patients during deep brain stimulation. *NPJ Parkinsons Dis*. 2022;8:88. doi: 10.1038/s41531-022-00350-7

16 Stam MJ, van Wijk BCM, Sharma P, *et al.* A comparison of methods to suppress electrocardiographic artifacts in local field potential recordings. *Clinical Neurophysiology*. 2023;146:147–61. doi: 10.1016/j.clinph.2022.11.011

17 Neumann W-J, Sorkhabi MM, Benjaber M, *et al.* The sensitivity of ECG contamination to surgical implantation site in brain computer interfaces. *Brain Stimulation: Basic, Translational, and Clinical Research in Neuromodulation*. 2021;14:1301–6. doi: 10.1016/j.brs.2021.08.016

18 Chen Y, ma B, Hao H, *et al.* Removal of Electrocardiogram Artifacts From Local Field Potentials Recorded by Sensing-Enabled Neurostimulator. *Frontiers in Neuroscience*. 2021;15. doi: 10.3389/fnins.2021.637274

19 Toth R, Zamora M, Ottaway J, *et al.* DyNeuMo Mk-2: An Investigational Circadian-Locked Neuromodulator with Responsive Stimulation for Applied Chronobiology. *Conf Proc IEEE Int Conf Syst Man Cybern*. 2020;2020:3433–40. doi: 10.1109/SMC42975.2020.9283187

20 Zamora M, Toth R, Morgante F, *et al.* DyNeuMo Mk-1: Design and pilot validation of an investigational motion-adaptive neurostimulator with integrated chronotherapy. *Exp Neurol*. 2022;351:113977. doi: 10.1016/j.expneurol.2022.113977

21 Deli A, Toth R, Zamora M, *et al.* The Design of Brainstem Interfaces: Characterisation of Physiological Artefacts and Implications for Closed-loop Algorithms. *Int IEEE EMBS Conf Neural Eng*. 2023;2023:10123850. doi: 10.1109/NER52421.2023.10123850

22 Swamy CP, Besheli BF, Branco LRF, *et al.* Pulsation artifact removal from intra-operatively recorded local field potentials using sparse signal processing and data-specific dictionary. *Annual International Conference of the IEEE Engineering in Medicine and Biology Society IEEE Engineering in Medicine and Biology Society Annual International Conference*. 2023;2023:1. doi: 10.1109/EMBC40787.2023.10340160

23 Goyal A, Goetz S, Stanslaski S, *et al.* The development of an implantable deep brain stimulation device with simultaneous chronic electrophysiological recording and stimulation in humans. *Biosens Bioelectron*. 2021;176:112888. doi: 10.1016/j.bios.2020.112888

24 Sanger ZT, Henry TR, Park MC, *et al.* Neural signal data collection and analysis of Percept™ PC BrainSense recordings for thalamic stimulation in epilepsy. *J Neural Eng*. 2024;21. doi: 10.1088/1741-2552/ad1dc3

25 NeuroPace, Inc. The NeuroPace RNS System for Responsive Neurostimulation: Exhibit C – Company Materials. Mountain View, CA: NeuroPace, Inc. Available from: https://braininitiative.nih.gov/sites/default/files/documents/ppp_rns_device_info_508c.pdf [Accessed 6 Feb 2026]

26 Ramanathan RS, Ahluwalia T, Sharma A. Lennox-Gastaut syndrome: An overview. *J Pediatr Neurosci*. 2010;5:86–8. doi: 10.4103/1817-1745.66666

27 Cucciolini G, Motroni V, Czosnyka M. Intracranial pressure for clinicians: it is not just a number. *Journal of Anesthesia, Analgesia and Critical Care*. 2023;3:31. doi: 10.1186/s44158-023-00115-5

28 Frohlich J, Toker D, Monti MM. Consciousness among delta waves: a paradox? *Brain*. 2021;144:2257–77. doi: 10.1093/brain/awab095

29 Chae I, Jeong CK, Ounaies Z, *et al.* Review on Electromechanical Coupling Properties of Biomaterials. *ACS Appl Bio Mater*. 2018;1:936–53. doi: 10.1021/acsabm.8b00309

30 Hermes D, Wu H, Kerr AB, *et al.* Measuring brain beats: Cardiac-aligned fast functional magnetic resonance imaging signals. *Human Brain Mapping*. 2023;44:280–94. doi: 10.1002/hbm.26128

31 Wagshul ME, Eide PK, Madsen JR. The pulsating brain: A review of experimental and clinical studies of intracranial pulsatility. *Fluids Barriers CNS*. 2011;8:5. doi: 10.1186/2045-8118-8-5

32 D'Antona L, Craven CL, Bremner F, *et al.* Effect of position on intracranial pressure and compliance: a cross-sectional study including 101 patients. *Journal of Neurosurgery*. 2021;136:1781–9. doi: 10.3171/2021.6.JNS203573

33 Lecchini-Visintini A, Zwanenburg JJM, Wen Q, *et al.* The pulsing brain: state of the art and an interdisciplinary perspective. *Interface Focus*. 2025;15:20240058. doi: 10.1098/rsfs.2024.0058

34 Almudayni A, Alharbi M, Chowdhury A, *et al.* Magnetic resonance imaging of the pulsing brain: a systematic review. *MAGMA*. 2023;36:3–14. doi: 10.1007/s10334-022-01043-1

35 Sawyer PN, Himmelfarb E, Lustrin I, *et al.* Measurement of Streaming Potentials of Mammalian Blood Vessels, Aorta and Vena Cava, in Vivo. *Biophysical Journal*. 1966;6:641–51. doi: 10.1016/S0006-3495(66)86683-3

36 Andresen M, Hadi A, Petersen LG, *et al.* Effect of postural changes on ICP in healthy and ill subjects. *Acta Neurochir*. 2015;157:109–13. doi: 10.1007/s00701-014-2250-2

37 Sagirov AF, Sergeev TV, Shabrov AV, *et al.* Postural influence on intracranial fluid dynamics: an overview. *Journal of Physiological Anthropology*. 2023;42:5. doi: 10.1186/s40101-023-00323-6

38 Bancroft MJ, Moncur EM, Peters AL, *et al.* Intracranial pressure and pulsatility in different head and body positions. *Brain Commun*. 2025;7:fcaf115. doi: 10.1093/braincomms/fcaf115